Journal of Aerosol Science 169 (2023) 106129

Contents lists available at ScienceDirect

Journal of Aerosol Science

journal homepage: www.elsevier.com/locate/jaerosci

Modeling oil–mist filtration through coalescence filter media in the presence of gravity-induced flows

M. Starnoni

Department of Civil and Environmental Engineering, Universitat Politecnica de Catalunya, Spain

ARTICLE INFO

Editor: Dr. Chris Hogan

Keywords:
Filtration
Coalescence filters
Oil–mist
Gravity
Gravity channels
Saturation

ABSTRACT

This paper jointly addresses numerical and physical challenges related to the modeling of coalescence filtration through vertical filter cartridges, put forth in the following papers by Starnoni, M. and C. Manes:

• Starnoni, M., & Manes, C. (2021). A multiphase multicomponent flow and transport model for liquid aerosol filtration in coalescence fibrous filters. *Separation and Purification Technology*, 266, 118574.

• Starnoni, M., & Manes, C. (2022). On the interplay between pressure and gravitational forces in coalescence filters. *Journal of Aerosol Science*, 105953.

In particular, it provides the multidimensional extension of the one-dimensional model presented in Starnoni and Manes (2021) to the general case where internal gravity-induced flows play an effective role. Key to the implementation is the decomposition of the moving oil volumes along the different directions proportionally to the dimensionless number S_M, a new quantity introduced in Starnoni and Manes (2022) describing the interplay between the forces dictating the oil dynamics. To validate the implementation, an experimental setup available in the literature is replicated, showing very good agreement in terms of all relevant quantities, namely saturation, pressure drop and drainage volumes. A generalized 'Network, Channel and Film' model is also formulated, which extends the scope of application of the original Jump and Channel model by Kampa et al. (2014) to filters with coarser fibrous microstructure. In particular, the existence of an additional flow mechanism termed 'network' is postulated, which is characterized by a complex multidimensional oil patterns configuration spanning the entire filter's height and evolving, in a macroscopic sense, along the direction identified by S_M.

1. Introduction

Coalescence fibrous filters are used in a variety of industrial applications to clean potentially hazardous aerosols of lubricating oil produced during operation (see Mead-Hunter et al. (2014) for a comprehensive review on aerosol-mist coalescence filters).

Numerical modeling of coalescence filtration is extremely complex and models to date had necessarily to make approximations (both at the conceptual and numerical level) in order to reach an optimum balance between model accuracy and computational effort. Available models mainly fall into two categories: pore-scale models (Azarafza et al., 2020; Mead-Hunter et al., 2013) and Darcy-scale models (Baumann et al., 2020; Starnoni & Manes, 2021). Herein, the latter category is considered. In particular, the focus is on the model by Starnoni and Manes (2021), which is the numerical transposition of the Jump & Channel (J&C) model by Kampa et al. (2014), and, to the author's best knowledge, the only available Darcy-scale model which properly accounts for all relevant oil transport mechanisms, including droplet capture, channel-like flow, film formation and associated pressure build up.

E-mail address: michele.starnoni@upc.edu.

https://doi.org/10.1016/j.jaerosci.2022.106129
Received 27 October 2022; Received in revised form 19 December 2022; Accepted 19 December 2022
Available online 22 December 2022
0021-8502/© 2022 The Author(s). Published by Elsevier Ltd. This is an open access article under the CC BY-NC-ND license (http://creativecommons.org/licenses/by-nc-nd/4.0/).

List of Symbols

Subscripts/superscripts

$+, -$	Used for detached volumes moving out from (−) and into (+) a control volume
0	Relative to initial dry conditions
$1,2$	Used for oil saturation relative to fibers (1) or coalescence (2)
δ	Relative to the oil film
ℓ	Relative to the ℓ-particle size
η	Used for mass exchange term relative to fiber efficiency
ψ	Used for mass exchange term relative to detachment
Σ	Total
$\star$	Normalized quantity
F	Relative to the filter
f	Relative to the fibers
g	Relative to the mist phase
i	Relative to the i-the element
in	Relative to the inflow
j	Relative to the jth layer
o	Relative to the oil phase
out	Relative to the outflow
p	Relative to the oil droplets
ss	Relative to steady-state conditions
x, z	Used for volume decomposition along horizontal (x) and vertical (z) direction

Greek symbols

α	Packing density []
χ	Critical saturation ratio []
Δ	Grid size [m]
δ	Equivalent film thickness [m]
$\delta^\star$	Normalized equivalent film thickness []
γ	Exponent in oil film correction function
λ	Mobility [$\mathrm{Pa^{-1}s^{-1}}$]
μ	Viscosity [Pa s]
ω	Weighting coefficient
ϕ	Porosity []
ψ	Parametrized detachment term [$\mathrm{kg/m^3s}$]
ρ	Density [$\mathrm{kg/m^3}$]
σ	Surface tension [N/m]
θ	Angle of coalescence
ε	Exponent in relative permeability function
φ	Fractional flow function []

Roman symbols

$\boldsymbol{g}$	Acceleration due to gravity vector [$\mathrm{m/s^2}$]
$\boldsymbol{q}$	Darcy flux [m/s]
Δp	Pressure drop [Pa]
Δp_0	Initial pressure drop [Pa]
$\Delta p_{channel}$	Channel pressure drop [Pa]
Δp_{exit}	Exit capillary pressure [Pa]
Δp_{jump}	Jump pressure drop [Pa]
Δp_{ss}	Steady-state pressure drop [Pa]

At the current state-of-the-art, simulations using this model are limited to flat homogeneous filters with a very dense fibrous microstructure, such as those studied in Kampa et al. (2014), Raynor and Leith (2000), Contal et al. (2004) and most of the experimental research to date. These filter media are characterized by oil mass loading rates that can be considered reasonably

A_F	Filter rear surface [m^2]
b	General source/sink term [kg/m^3s]
b_η	Fiber efficiency term [kg/m^3s]
b_ψ	Detachment term [kg/m^3s]
c	Oil concentration [kg/m^3]
$c^\star$	Inlet concentration function []
c_{in}	Inlet oil concentration [kg/m^3]
D	Filter's width [m]
d_f	Fiber diameter [m]
d_p	Particle diameter [m]
g	Gravity constant [m/s^2]
H	Filter's height [m]
h_j	Height of jth layer [m]
i	Pressure gradient [Pa/m]
K	Filter's intrinsic permeability [m^2]
K_0	Filter's initial intrinsic permeability [m^2]
L	Filter's thickness [m]
l_c	Filter's characteristic length [m]
m	Oil mass loading per unit filter area [kg/m^2]
M_o	Oil mass [kg]
M_{in}	Injected oil mass [kg]
$M_{o,\delta}$	Oil film mass [kg]
$M_{o,\Sigma}$	Total oil mass [kg]
$M_{o,dr}$	Drainage oil mass [kg]
$M_{o,out}$	Outflow oil mass [kg]
N	Number of elements
p	Pressure [Pa]
p_{out}	Outflow reference pressure [Pa]
r_c	Characteristic pore size [m]
r_{in}	Inlet loading rate [kg/m^2s]
s	Saturation []
S_e	Equilibrium saturation []
S_M	Ratio of pressure to gravitational forces [dimensionless]
S_o	Filter saturation []
$s_{o,1}$	Saturation of oil attached to the fibers []
$s_{o,2}$	Saturation of mobile coalesced oil []
$s_{o,cr}$	Critical Saturation []
t	Time [s]
t_0	Initial time at dry conditions [s]
t_δ	Start time of oil film creation [s]
$t_{channel}$	Start time of Kampa-like oil movement [s]
t_{detach}	Start time of oil movement [s]
t_{ss}	Establishment of oil pseudo steady-state [s]
V_F	Filter volume [m^3]
v_{in}	Inlet velocity [m/s]
$V_{o,out}$	Outflow volume [m^3]
$\Delta p^\star$	Pressure drop ratio []

homogeneous over the entire front face and, most importantly, a very dense fibrous microstructure that very likely inhibits internal vertical flows, resulting in a homogeneous vertical oil distribution within the filter. These two features combined indicate that oil transport inside the filter essentially occurs along the direction of the air flow, say, the contribution of gravity to the flow is negligible, which motivated the use of the one-dimensional (1D) flow approximation in Starnoni and Manes (2021).

However, this assumption brings the filter cartridges typically used in industrially-relevant scenarios out of the scope of application of Starnoni and Manes (2021), as heterogeneous flow properties and associated oil mass transport rates are likely to

Other symbols

κ	Relative permeability []
$\mathcal{F}$	Oil film correction factor []

occur as a result of the complex interaction between the turbulent flow developing in the interior of the cartridge and operating conditions. This was emphasized in a recent publication by Starnoni and Manes (2022), where the authors tried to replicate an experimental setup available in the literature pertaining to a filter cartridge (Liu et al., 2016), yet without being able to reproduce the saturation profiles using the 1D approximation. This was because in these coarser fibrous media, gravity-induced flows internally to the filter play a major role, causing a vertical oil redistribution within the filter. In this context, a new dimensionless number, S_M, defined as the ratio between pressure and gravitational forces, that is

$$S_M = \frac{i}{\rho_o g} = \frac{pressure\ gradient}{gravitational}, \tag{1}$$

was introduced in Starnoni and Manes (2022) to provide a bulk characterization of the flow and assess whether internal gravity-induced flows, in a given cartridge-oil system, should be expected (and hence modeled) or not. It was shown that S_M explains well the few experimental data available in the literature and identifies specific behaviors associated with limiting S_M values being either very large or close to 1. Specifically, for $S_M \gg 1$, flow is essentially 1D and the model by Starnoni and Manes (2021) can be effectively used to simulate darcian-type flow through the filter's thickness. When instead $S_M \approx 1$, gravity-induced flows are vey likely to take place and hence the model by Starnoni and Manes (2021) can no longer be applied.

The scope of this paper is twofold. The first one is at the numerical level: To provide the additional operators needed to extend the 1D model by Starnoni and Manes (2021) to the general multidimensional case where oil transport occurs along multiple direction, specifically the incorporation of gravitational effects into the darcian flow model and the associated parametrization of gravity-induced flows. To validate the implementation, the same experimental setup by Liu et al. (2016) is replicated, this time showing very good agreement in terms of all relevant quantities, namely pressure drop, saturation and drainage volumes.

The second contribution of this paper is at the conceptual level: To generalize the original J&C model by Kampa et al. (2014) to the general case where filters can have a coarser fibrous microstructure. In fact, the original J&C model is built on the assumption that liquid propagates as a vertical front in the direction of the air flow (Kampa et al., 2014). However, the saturation profiles detected in Liu et al. (2016) clearly show that coalesced oil does not propagate so, at least during the initial stages of loading, but instead redistributes vertically within the filter due to gravity. A third mechanism of oil transport induced by both the air flow and gravity is therefore introduced herein in addition to the original jump and channel mechanisms. This additional mechanism will be termed "network" and is characterized by a complex multidimensional oil patterns configuration spanning the entire filter's height and evolving, in a macroscopic sense, along the direction identified by S_M. It will be shown that the generalized "Network, Channel & Film" model explains very well the experimental evidence of Liu et al. (2016).

The paper is organized as follows. The mathematical model is presented in Section 2. Simulation results are presented and discussed in Section 3. The generalized Network, Channel & Film model is illustrated in Section 4. Finally, concluding remarks are given in Section 5.

2. Numerical method

Consider a filter of thickness L, height H, porosity ϕ and intrinsic permeability K. The filter is positioned vertically and the air flows along the horizontal direction. The filter is subdivided along the vertical direction into N_j layers of height h_j, for $j = 1, \dots, N_j$, as illustrated in the left panel of Fig. 1. Each layer is then treated as a 1D medium to which an equilibrium saturation $S_{e,j}$ and an inlet oil concentration $c_{in,j}$ is assigned. Note that $S_{e,j}$ is a property of the medium and operating conditions, while $c_{in,j}$ is calculated using the Eulerian–Lagrangian framework presented in Starnoni and Manes (2022). Now, as discussed in Starnoni and Manes (2022), there are two possible scenarios for the oil flow patterns internally to the filter based on the limiting values of S_M, as illustrated in the right panel of Fig. 1. In the one case, when $S_M \gg 1$, there are no internal gravity-induced flows, flow is essentially one-dimensional and there is no mass exchange between layers, hence each layer can be solved independently using the model presented in Starnoni and Manes (2021) without formal modifications. In the second case, when instead $S_M \approx 1$, there are internal flows due to gravity (and hence mass exchange between layers), therefore additional operators are needed. The scope of this section is indeed to introduce these operators and their discretization.

2.1. Governing equations

At the microscopic level, two phases coexist within the filter, namely the oil-mist phase, to which a subscript 'g' is associated, and the oil phase (subscript 'o'). These two phases are described in the mathematical model through the concept of phase saturation s, with the property that $s_g + s_o = 1$. Specifically, the oil-mist phase is composed by a mixture of a gas phase and a concentration of oil droplets of different sizes ℓ (with the assumption that the inlet oil concentration is low enough to take the mist density and viscosity as equal to those of the gas phase). Oil is present in three forms during operation: (i) individual droplets inside the mist,

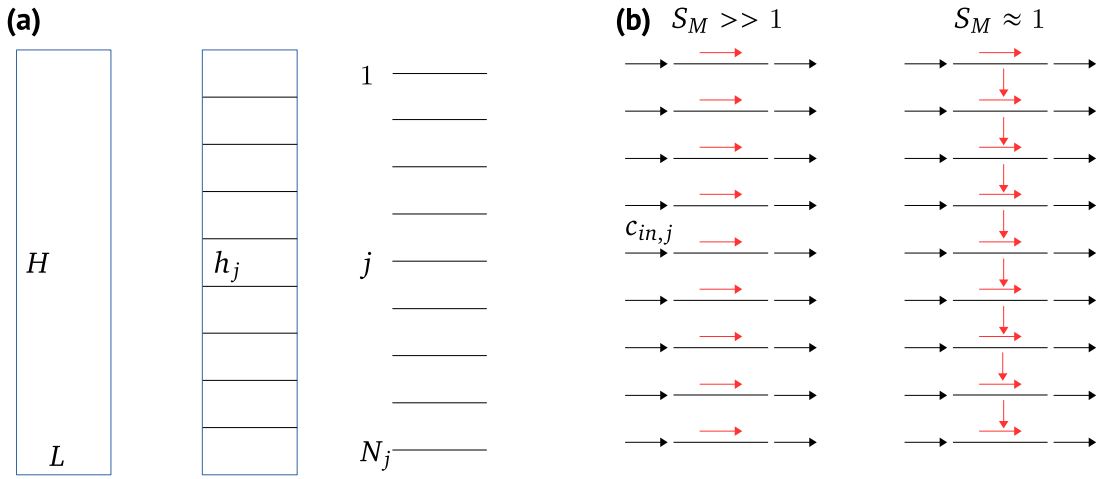

Fig. 1. (a) Subdivision of a filter along the vertical direction into N_j layers of height h_j, for $j = 1, N_j$, and (b) schematization of the oil flow patterns internally to the filter based on the limiting values of the S_M number.

(ii) individual droplets attached to the fibers and (iii) coalesced oil moving within the filter (in all directions). The transition from one form to another is represented in the model through ad hoc mass exchange terms b, which have the units of mass rates per unit volume [kg m^{-3} s^{-1}] and act like sources/sinks for the control volume. For example, the transition from form (i) to form (ii) is given by the fiber efficiency term b_η, while the transition from form (ii) to form (iii) is given by the detachment terms $b_\psi^\pm$. In particular, $b_\psi^\pm$ are activated once a certain critical saturation value is reached locally and represent the amount of oil dropping into (superscript +) and out from (−) a control volume, respectively, during the time interval.

The governing equations for the control volume are then written as follows:

$$\phi \frac{\partial s_o}{\partial t} + \nabla \cdot \boldsymbol{q}_o = \frac{1}{\rho_o}\left(\sum_\ell b_{\eta,\ell} + b_\psi^+ - b_\psi^-\right) \tag{2}$$

$$\phi \frac{\partial}{\partial t}\left(c_\ell s_g\right) + \nabla \cdot \left(c_\ell \boldsymbol{q}_g\right) = -b_{\eta,\ell} \qquad for\ all\ \ell \tag{3}$$

$$\phi \frac{\partial s_g}{\partial t} + \nabla \cdot \boldsymbol{q}_g = -\frac{1}{\rho_g}\sum_\ell b_{\eta,\ell} \tag{4}$$

$$\boldsymbol{q}_g = -\frac{\kappa_g(s_g)}{\mu_g} K \nabla p \tag{5}$$

$$\boldsymbol{q}_o = -\frac{\kappa_o(s_o)}{\mu_o} K \left(\nabla p - \rho_o \boldsymbol{g}\right) \tag{6}$$

Here, t is time, $\boldsymbol{q}_\alpha$ (with $\alpha = g, o$) are the Darcy fluxes, ρ and μ are the density and viscosity, respectively, c_ℓ is the concentration of oil droplets of size ℓ, p is pressure (which, in absence of capillary forces, is assumed to be the same for both phases), $\boldsymbol{g}$ is the acceleration due to gravity vector, and κ_α are the relative permeabilities (which are taken as functions of the respective saturations). Note that in Eq. (5) the contribution of gravity to the flux of the gas phase is neglected for obvious reasons.

Introducing the phase mobilities λ_α, defined as

$$\lambda_\alpha = \frac{\kappa_\alpha}{\mu_\alpha}, \tag{7}$$

summing Eqs. (2) and (4), the pressure equation is obtained in the following form:

$$-\nabla \cdot \left[K\left(\lambda_\Sigma \nabla p - \lambda_o \rho_o \boldsymbol{g}\right)\right] = \left(\frac{1}{\rho_o} - \frac{1}{\rho_g}\right)\sum_\ell b_{\eta,\ell} + \frac{1}{\rho_o}\left(b_\psi^+ - b_\psi^-\right), \tag{8}$$

where λ_Σ is the total mobility, defined as the sum of the phase mobilities, i.e. $\lambda_\Sigma = \lambda_g + \lambda_o$.

Let us now partition the oil saturation s_o into its two constitutive forms, namely $s_{o,1}$ and $s_{o,2}$, such that $s_o = s_{o,1} + s_{o,2}$. Of these, $s_{o,1}$ is the oil attached to the fibers, which is immobile – that is, $\boldsymbol{q}_{o,1} = 0$, while $s_{o,2}$ is the coalesced oil which is flowing inside the medium – that is, $\boldsymbol{q}_o = \boldsymbol{q}_{o,2}$. Hence, the mass conservation equation of the coalesced oil, Eq. (2), is split into two components as follows:

$$\phi \frac{\partial s_{o,1}}{\partial t} = \frac{1}{\rho_o}\left(\sum_\ell b_{\eta,\ell} - \omega_1 b_\psi^-\right) \tag{9}$$

$$\phi \frac{\partial s_{o,2}}{\partial t} + \nabla \cdot \boldsymbol{q}_o = \frac{1}{\rho_o}\left(b_\psi^+ - \omega_2 b_\psi^-\right) \tag{10}$$

where ω_β (with $\beta = 1, 2$) are weighting coefficients (with the property that $\omega_1 + \omega_2 = 1$). These coefficients, which are introduced for stability reasons, account for the fact that oil sinks can be due to coalesced oil droplets either detaching from the fibers or deviating their path from the channels, and are calculated proportionally to the respective sub-saturations in the following manner:

$$\omega_\beta = \frac{s_{o,\beta}}{s_o}.$$

On the contrary, all sources contribute to $s_{o,2}$ – that is, detachment is an irreversible process. Finally, the flux of the coalesced oil, $\boldsymbol{q}_o$, is activated when $s_{o,2} \neq 0$, and is calculated using Darcy's law with a relative permeability taken as a function of $s_{o,2}$ only, that is, in Eq. (6), one has that:

$$\kappa_o = \kappa_o(s_{o,2}). \tag{11}$$

Applying a fractional flow formulation, Eq. (10) is then rewritten as

$$\phi \frac{\partial s_{o,2}}{\partial t} + \nabla \cdot \left(\varphi_o \left(\boldsymbol{q}_\Sigma - \lambda_g K \rho_o \boldsymbol{g} \right) \right] = \frac{1}{\rho_o} \left(b_\psi^+ - \omega_2 b_\psi^- \right), \tag{12}$$

where $\boldsymbol{q}_\Sigma$ is the total flux, i.e. $\boldsymbol{q}_\Sigma = \boldsymbol{q}_g + \boldsymbol{q}_o$, and φ_o is the fractional flow function defined as $\varphi_o = \lambda_o / \lambda_\Sigma$. Eqs. (8)–(9)–(12) form a system of three equations for three principal unknowns (namely p, $s_{o,1}$ and $s_{o,2}$) which is solved using the multipoint flux approximation scheme outlined in Starnoni et al. (2019).

2.2. Discretization of the mass exchange terms

With reference to Fig. 1, consider the generic jth layer, which is discretized in the horizontal direction into N_i elements. Consider the time station at which the generic internal ith cell (with $i = 1, \dots, N_i$) has reached its critical saturation, that is $s_{o,j,i} \geq s_{o,cr,j,i}$. Contrary to the Kampa-like filters for which $S_M \gg 1$ and flow is essentially one-dimensional, the coalesced oil detaching from the fibers, b_ψ^-, will now move in both directions. A question thus naturally arises: how much oil will move horizontally driven by the pressure gradient and how much will redistribute vertically due to gravity? In the spirit of the S_M number, sinks out from the (i, j)-th cell in the horizontal (subscript x) and vertical (subscript z) directions, respectively, are assigned which are proportional to the respective driving forces in the following manner:

$$b_{\psi,x}^- = \psi \cos\theta, \tag{13}$$

$$b_{\psi,z}^- = \psi \sin\theta, \tag{14}$$

where the (i, j) indices are omitted for clarity. Here, θ is the angle of coalescence defined as:

$$\theta = \arctan \frac{1}{S_M}, \tag{15}$$

and ψ is the detachment mass rate (per unit volume) parametrized following Raynor and Leith (2000) as

$$\psi = \chi \frac{\rho_o \sigma}{\mu_o \Delta},$$

where σ is the surface tension, Δ is the size of the (i, j)-th cell and χ is the critical saturation ratio defined as

$$\chi = \ln \frac{s_o}{s_{o,cr}}.$$

For mass continuity, one also has that, for all $i \neq 1$ and $j \neq N_j$:

$$b_{\psi,x}^+(j,i) = b_{\psi,x}^-(j,i-1) \qquad \text{and} \qquad b_{\psi,z}^+(j,i) = b_{\psi,z}^-(j-1,i).$$

Full account of the parametrization of $s_{o,cr}$, b_η and ψ, as well as a detailed description of the time and space discretization schemes adopted, can be found in Starnoni and Manes (2021).

Two features of the generalized model as presented herein are additionally pinpointed. Firstly, when $S_M \gg 1$, that is, when $\nabla p \gg \rho_o g$, one has that

$$\theta \to 0, \qquad b_{\psi,x}^- \to \psi, \qquad b_{\psi,z}^- \to 0,$$

and the whole formulation reduces to the 1D case outlined in Starnoni and Manes (2021). This normally occurs for dense fiberglass filter media, where the intrinsic permeability is very low, but can also be the case of relatively open-pore filter media at relatively high filtration velocities, where the drag force on moving coalesced oil (and hence the pressure gradient) is high. Secondly, only one additional model parameter is introduced herein, namely the relative permeability κ_o in Eq. (6), which is taken as a function of the coalesced oil saturation $s_{o,2}$ as given in Eq. (11). This functional relationship is expressed, in analogy with its gas phase counterpart, through a power law of the form:

$$\kappa_{o,j} = s_{o2,j}^{\varepsilon_o(j,t)}, \tag{16}$$

where the exponent ε_o is a function of time and position along the filter's height. We shall return to the parametrization of κ_o later on the paper.

Table 1
Properties of the filter used in the simulations. Data taken from the experimental setup of Liu et al. (2016).

Parameter	Description	Value	Units
L	Filter's thickness	17	mm
H	Filter's height	900	mm
α	Packing density	0.18	
K_0	Intrinsic permeability	100	Da
d_f	Fiber diameter	25	μm
d_p	Volume median particle diameter	4.2	μm
ρ_o	Oil density	960	kg m^{-3}
ρ_g	Gas density	1	kg m^{-3}
μ_g	Gas dynamic viscosity	$1e^{-5}$	Pa s
μ_o	Oil dynamic viscosity	0.1	Pa s
σ	Surface tension	0.03	N m^{-1}
v_{in}	Inlet velocity	0.1	m s^{-1}
c_{in}	Oil mass inlet concentration	300	mg m^{-3}
p_{out}	Outflow reference pressure	0	mbar
Δp_{exit}	Exit capillary pressure	10	mbar

2.3. Enhanced treatment of the oil film

In Starnoni and Manes (2021), the oil film forming at the rear end of the (oleophilic) filter was modeled as the saturation of the rear end cell. In this manner, drainage out from the outflow boundary was inhibited until the exit capillary pressure was overcome, and the oil accumulation at the rear end of the filter was effectively modeled. The associated permeability reduction as a function of the film saturation was then modeled through a correction factor $\mathcal{F}$ in the following manner:

$$K = \mathcal{F} K_0, \tag{17}$$

where K_0 is the initial permeability at conditions of dry filter and $\mathcal{F}$ was defined in Starnoni and Manes (2021) as:

$$\mathcal{F} = (1 - s_{o,N_i})^{\gamma}, \tag{18}$$

with γ a positive material constant and s_{o,N_i} the saturation of the rear end cell.

However, this results in a mesh dependency issue, as, with increasing mesh resolution, the film saturation increases dramatically, since the same drainage volume is contained in a progressively smaller cell. This can severely affect the accuracy of the predicted pressure drop, as the rise in jump pressure drop can become very steep for very small grid size. To fix this issue, herein the oil is let free to drain out from the outflow surface and track of the outflow volume is kept by means of an equivalent film thickness δ defined as:

$$\delta = \frac{V_{o,out}}{A_F}, \tag{19}$$

where $V_{o,out}$ is the outflow volume and A_F is the filter rear surface. The outflow volume is calculated as a function of time in the following manner:

$$V_{o,out}(t) = A_F \int_o^t \left(b^-_{\psi,N_i} \Delta + q_{o,out} \right) dt, \tag{20}$$

where b^-_{ψ,N_i} is the detached volume of the rear cell and $q_{o,out}$ is the oil flux at the outflow boundary.

The correction factor $\mathcal{F}$ is then calculated from a normalized equivalent film thickness $\delta^\star$ as follows:

$$\mathcal{F} = \left(1 - \delta^\star\right)^{\gamma}, \qquad \delta^\star = \frac{\delta}{l_c} \tag{21}$$

where l_c is a characteristic length for the filtering material. In this work, l_c is taken equal to 0.5 mm, corresponding to the thickness of the basic constitutive filter layer (note that coalescence filters typically consist of multiple layers of fibrous media). When exit capillary forces are overcome, the current value of the equivalent film thickness δ is stored and kept unchanged in the remainder of the calculations. Note that this relation between the growing film thickness and the build up of the pressure drop is still an open research question and should be subject of further research.

3. Numerical example and discussion

Here, the experimental setup of Liu et al. (2016) ($S_M \approx 1$) is replicated. This is the same experimental setup for which the 1D approximation was shown to produce inconsistent saturation profiles along the filter's height, as reported in Starnoni and Manes (2022). It is therefore expected the generalized multidimensional model presented herein, with extended capabilities to account for oil redistribution within the filter due to gravitational effects, be able to replicate the saturation profiles detected in Liu et al. (2016).

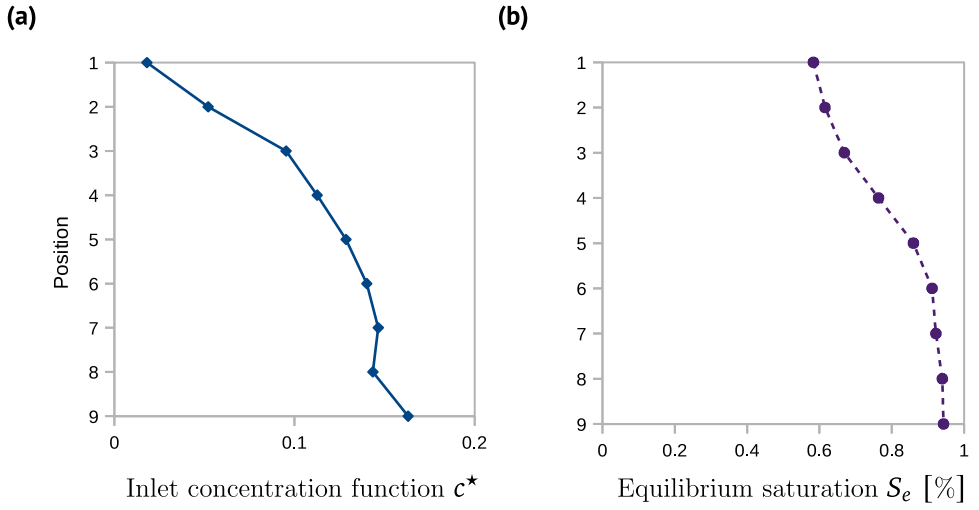

Fig. 2. Vertical distribution of (a) the inlet concentration function $c^\star$ and (b) equilibrium saturation S_e. The inlet concentration function is the result of the simulations presented in Starnoni and Manes (2022), while the equilibrium saturations are extracted from Liu et al. (2016).

3.1. Numerical setup

The filter is partitioned into nine layers along the vertical direction ($N_j = 9$), which are numbered from 1 (top) to 9 (bottom) as in Liu et al. (2016). The nine layers have the same height $h_j = 100$ mm (for $j = 1, \dots, 9$). A grid of $N_i = 50$ cells is used ($\Delta = 0.34$ mm) along the filter's thickness, which is fine enough for the results to be mesh-independent. Initially, the filter is clean, that is $s_o(\boldsymbol{x}, t = 0) = 0$. For simplicity, it is assumed that all oil droplets have the same diameter d_p, thus a single concentration equation is solved for a single value of c. Boundary conditions for the flow problem consist of an applied velocity v_{in} at the inflow boundary and a reference pressure p_{out} at the outflow boundary. For the transport problem, an inlet loading rate $r_{in,j}$ is applied to the jth inflow boundary, which is calculated as

$$r_{in,j} = c_{in} c_j^\star v_{in} N_j,$$

where c_{in} and v_{in} are the global oil mass inlet concentration and filtration velocity, respectively, and $c^\star$ is the inlet concentration function (with the property that $\sum_j c_j^\star = 1$) taken as output from the Eulerian–Lagrangian simulations carried out in Starnoni and Manes (2022) (see Fig. 2(a)). Boundary conditions are consistent with the aerosol generated in Liu et al. (2016), specifically $v_{in} = 0.1$ m/s and $c_{in} = 300$ mg/m^3. Also, no drainage out from the bottom layer is allowed but at its rear face, which is consistent with the technical specifications of the filter cartridge used in Liu et al. (2016).

The model further needs two material parameters describing oil transport inside the medium, namely the global equilibrium saturation S_e (as a function of the filter's height) and the exit capillary pressure Δp_{exit}. The former is directly taken from the steady-state saturation profile detected in Liu et al. (2016) (see Fig. 2(b)). The latter is set to 10 mbar, a value estimated using the Young–Laplace equation

$$\Delta p_{exit} = 2\frac{\sigma}{r_c},$$

where σ is the surface tension and r_c is a characteristic pore size taken equal to 50 μm. This value of r_c is taken from the drainage layer reported in Chang et al. (2016), a material with very similar properties of that used in Liu et al. (2016) and which visually fits the pressure drop curve detected in Liu et al. (2016). All data for the simulations are summarized in Table 1.

Finally, the relative permeability of the oil phase is taken as a function of time and position along the filter's height through the exponent ε_o in Eq. (16). Notably, ε_o is the only additional free parameter introduced in the model presented herein, and its values used in the calculations are reported in Fig. 3. The fact that ε_o varies throughout the filtration process is in line with the observations of Kolb et al. (2017) who have shown that, for the gas phase, ε_g varies between 1 and 4.55, depending on the actual oil configuration inside the filter. Hence, it is assumed here that the same applies to the oil phase. Moreover, as pointed out in Kampa et al. (2015), the moving oil does not form a continuous moving front but rather a succession of coalesced oil drops moving along the same preferred pathways, suggesting that the oil relative permeability may vary at least until these preferential pathways are established along the entire filter's height and through the entire filter's thickness—in our case, this seemingly occurs after the second flow interruption in Liu et al. (2016). An exact determination of these relative permeabilities functions would require a proper parametrization of the relevant material, which is not always readily available for fiber media and is certainly beyond the scope of the present work.

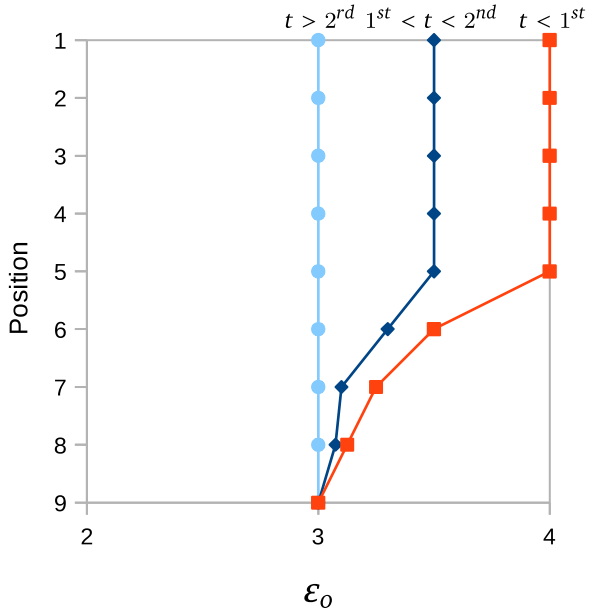

Fig. 3. Values of the exponent ϵ_o in Eq. (16) as a function of time and position along the filter's height.

3.2. Pressure drop

Following the Jump and channel model by Kampa et al. (2014), the total pressure drop Δp is given by three contributions, namely the initial pressure drop at conditions of dry filter, Δp_0, the channel pressure drop, $\Delta p_{channel}$, and the jump pressure drop, Δp_{jump}. The channel pressure drop is related to Δp_0 via the increase in Darcy flux of the gas phase as follows:

$$\frac{\Delta p_{channel}}{\Delta p_0} = \frac{1}{(1-s_o)^{\epsilon_g}}, \tag{22}$$

while Δp_{jump} is related solely to the capillary properties of the medium and fluids (Kampa et al., 2015). In order to highlight this decomposition and better visualize the net pressure drop due to oil loading, it is customary in the coalescence literature to report the pressure drop ratio $\Delta p^\star$, which is defined in Liu et al. (2016) as

$$\Delta p^\star = \frac{\Delta p - \Delta p_0}{\Delta p_{ss} - \Delta p_0}, \tag{23}$$

where Δp_{ss} is the pressure drop at steady-state.

Figs. 4(a) and 4(b) report the evolution of the calculated Δp and $\Delta p^\star$, respectively, in the bottom layer as compared to the experimental values. Note that this comparison is shown in layer 9 only, as it is the location where the pressure drop is measured in Liu et al. (2016). Besides, this location is where most of the oil accumulation occurs (and hence where the differential pressure mainly builds up). Note that, in order to be consistent with the results presented in Liu et al. (2016), the evolutions are shown in terms of mass loadings per unit filter area m rather then in time, with $m = c_{in} v_{in} t$.

As both figures clearly show, excellent agreement is achieved between numerical and experimental values. Note that the filter studied in Liu et al. (2016) features a net pressure drop which is almost entirely given by Δp_{jump}, say $\Delta p_{channel} \approx 0$. Specifically, $\Delta p^\star$ is nearly zero during the wetting stage until the first flow interruption (say, until $m = 0.05$ kg/m^2), i.e. the internal saturations are so low that the channel pressure drop is almost negligible. What triggers the pressure build up is obviously the formation of the oil film at the rear end of the filter. This is clearly illustrated in Fig. 4(b), where the normalized equivalent film thickness $\delta^\star$, calculated using Eq. (21), is reported to facilitate interpretation of results. It is striking to see that the model is able to capture the two-stages of the pressure build-up (note the small kink in Fig. 4(a) at $m \approx 0.075$ kg/m^2). This small kink corresponds to a change in slope of the film thickness (see Fig. 4(b)) and is a first clue that a change in oil dynamics is taking place around this time. Specifically, for values of m greater than ≈ 0.075 kg/m^2, the oil film dynamics becomes slower in the bottom layer because oil is now retained in the upper layers instead of draining downwards and accumulating in the bottom layer. This is due to an enhanced oil mobilization in the upper layers, presumably caused by the complete formation of the "Kampa"-like channels[1] – a feature that will be explored in much greater detail in the following. The increase in pressure drop naturally terminates when Δp_{exit} is overcome, and steady-state is locally established.

[1] For "Kampa"-like channels, it is intended that oil propagates as a vertical front in the direction of the air flow, i.e. the mechanisms of oil transport are induced by the air flow, with gravity playing no role.

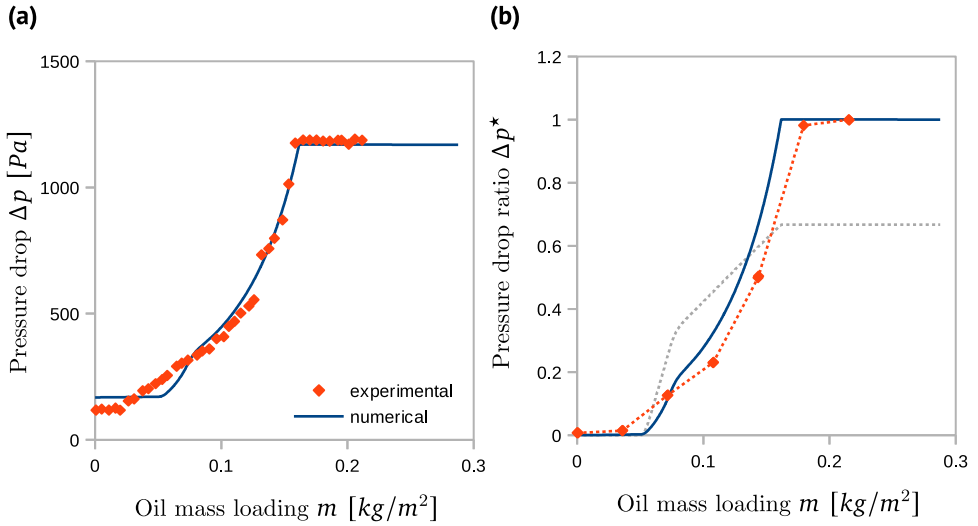

Fig. 4. Evolution of the pressure drop (a) and pressure drop ratio (b) in layer 9. Experimental values are extracted from Liu et al. (2016). The dashed gray line in (b) is the normalized equivalent film thickness $\delta^{\star}$ in layer 9, calculated using Eq. (21).

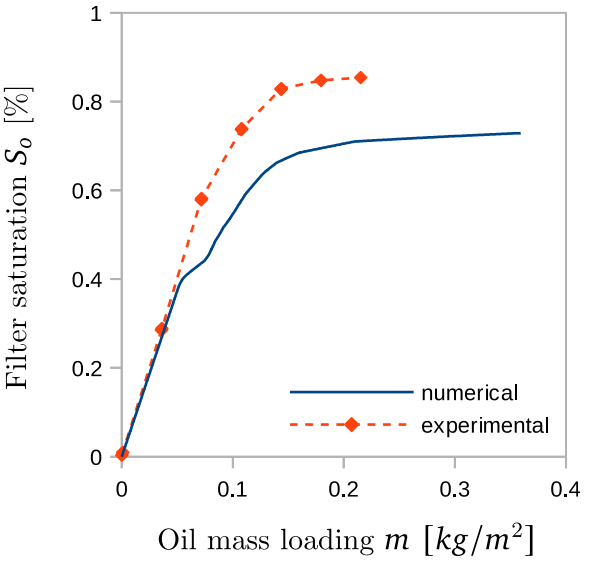

Fig. 5. Saturation of the whole filter as a function of the oil mass loading. Experimental values are extracted from Liu et al. (2016). Numerical values are calculated using Eq. (24).

3.3. Saturation

3.3.1. Saturation of the whole filter

Consider first the saturation of the whole filter, S_o, which is calculated as

$$S_o = \frac{\sum_{i,j} s_{o,j,i} \Delta_i}{\sum_{i,j} \Delta_i} = \frac{\sum_{i,j} s_{o,j,i}}{N_i N_j}. \tag{24}$$

where Δ_i is the grid size and the sum is over all cells. S_o is reported in Fig. 5 as compared to the experimental values extracted from Liu et al. (2016). Generally, the experimental saturation is higher than the numerical one. This is mainly due to experimental artifacts during the weighing procedures. Specifically, the oil film at the rear surface of the filter is re-sucked back into the filter (due to capillary action) during the dismantling operations, resulting in an overestimated oil content. The film, in fact, is maintained only during filter operation and collapses as soon as the airflow is stopped and becomes absorbed in the filter, thereby causing a significant increase in local saturation (Kolb & Kasper, 2019). Indeed, as shown in Fig. 5, the experimental and numerical saturations

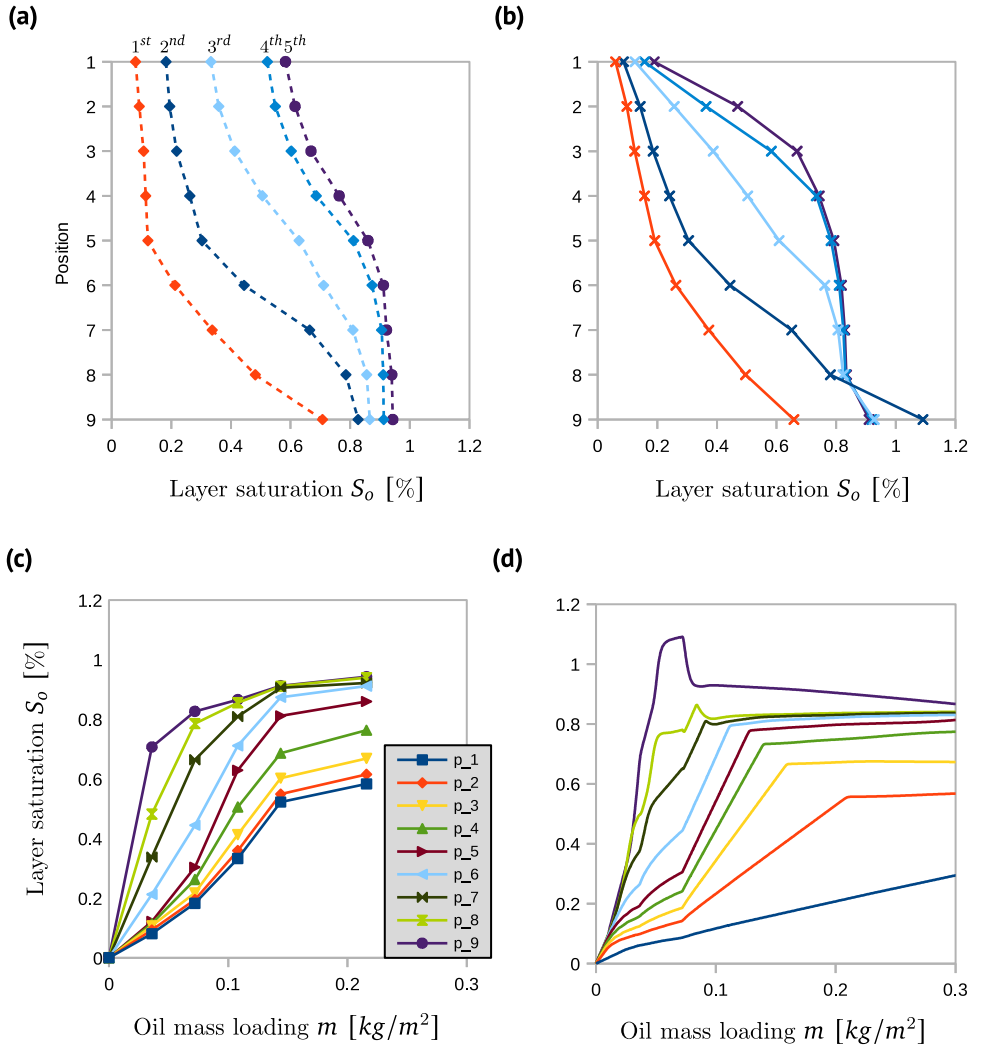

Fig. 6. Evolution of the saturation profiles at different positions along the filter's height. Experimental values in (a) and (c) are extracted from Liu et al. (2016). Numerical values in (b) and (d) are calculated using Eq. (25).

practically coincide during the initial wetting stage, that is, when the injected oil has not yet reached the rear surface of the filter and no oil film has yet formed. After that, the saturation deviates from linear wetting, as drainage out from the filter begins to take place.

Again note the inflection point in Fig. 5 at $m = 0.072$ kg/m^2 indicating that a change in oil dynamics is taking place. As discussed at the end of the previous section, it presumably reflects a change in oil configuration within the filter, specifically it identifies the complete formation of the oil channels, in the Kampa-like sense, in the middle and top sections of the filter. The complete formation of the Kampa-like channels induces a greater oil mobilization within these regions, causing oil to remain inside the original layers instead of redistributing vertically (and eventually draining out from the filter through the outflow surface of the bottom layer), thereby retaining a greater amount of oil inside the whole filter. As a consequence, the internal saturation increases globally while, on the contrary, the film thickness decreases locally at the rear face of the bottom layer (see Fig. 4(b)).

3.3.2. Layer saturations

The attention is now turned to the saturation profiles at each position along the filter's height. Fig. 6 compares the experimental and numerical saturation profiles at different time stages and at different positions along the filter's height, whereby the numerical saturation of the jth layer, $S_{o,j}$, is calculated as:

$$S_{o,j} = \frac{\sum_i s_{o,j,i} \Delta_i}{\sum_i \Delta_i} = \frac{\sum_i s_{o,j,i}}{N_i}. \tag{25}$$

where now the sum is only over the N_i cells across the filter's thickness. Time stages correspond to the five flow interruptions in Liu et al. (2016), corresponding to values of mass loading m of 0.036, 0.072, 0.108, 0.144 and $0.180\ \mathrm{kg/m^2}$, respectively.

As Fig. 6 clearly shows, good agreement is obtained between experimental and numerical values, demonstrating once again the predictive capabilities of the implementation. In particular, non-uniform oil saturation profiles are produced along the vertical direction, resembling the S-shape detected in Liu et al. (2016), with oil accumulating on the bottom section of the filter. Indeed, note that the curves corresponding to the first two flow interruptions are those featuring the more uneven saturation distributions. As explained in Starnoni and Manes (2022), this is likely due to the combined effects of heterogeneous loading rates on the filter's front surface (caused by the heterogeneity of the complex flow fields developing in the interior of the filter cartridge) and internal gravity-induced flows. This also seemingly suggests that channels are not yet established in the upper layers until the second flow interruption, at least not in the Kampa-like sense, with oil from those layers mainly migrating vertically towards the bottom section of the filter.

In particular, giving a closer look at the experimental curves (Figs. 6(a) and 6(c)), it seems rather obvious that there is a change in the oil transport processes after the second flow interruption. Specifically, the saturation profiles along the filter's height reported in Fig. 6(a) (experimental data extracted from the left panel of figure 10 of Liu et al. (2016)) appear to shift uniformly towards the right after the second flow interruption rather than keeping distorting towards the bottom as the curves detected for the first two measurements. Likewise, the saturations reported in Fig. 6(c) (experimental data extracted from the right panel of figure 10 of Liu et al. (2016)) exhibit a steep increase in the middle and top layers (say, from P1 to P5) after the second flow interruption. We shall return to this change in oil dynamics in the next section.

In general, the numerical saturation profiles are consistent with the experimental profiles detected in Liu et al. (2016). Specifically, the liquid saturations of the upper layers (say, from P2 to P5) exhibit an S-shape, while the curves of the bottom layers (P6 to P9) have a smoother parabolic profile. Note that these features are reproduced in the numerical model through the relative permeability function taken as a function of time and position along the filter's height, as discussed at the end of Section 3.1. Notably, the change in oil dynamics after the second flow interruption is rather abrupt in the numerical profiles as compared to the smoother experimental profiles of Liu et al. (2016), as in the calculations relative permeability changes from one time step to another. To this end, additional research is certainly needed here, as coalescence will be studied more in-depth and improved $\kappa_o(s_o)$ relationships will be produced, either experimentally or using pore-scale numerical simulations such as those of Mead-Hunter et al. (2013).

Before moving forward, two minor discrepancies between the experimental and numerical profiles are pinpointed. Firstly, at the end of the second flow interruption, the numerical saturation exhibits a greater accumulation at the bottom layer due to the effects of gravity-induced oil redistribution within the filter. This excess in oil accumulation, which is evident in both Figs. 6(b) and 6(d), disappears shortly after the second flow interruption, when channels are presumably established in the upper layers and steady-state is locally established in the bottom layer. This excess of oil was not directly reported in the experimental curves detected in Liu et al. (2016), however the experimental measures of internal saturation are not continuous but require flow interruptions, as well as dismantling and weighing operations which are very difficult from a technical point of view, and which often result in artefacts. To this end, Liu et al. (2016) point out themselves that "the accuracy of the data is often in doubt, because the distribution of the liquid in filter layers changes as a result of the flow interruption". Hence, it cannot be a priori excluded that this oil excess is in fact due to take place but during a time interval which was not detected by Liu et al. (2016).

The second remark concerns the top layer, which always exhibits a lower saturation as compared to the experimentally measured values. Two possible explanations to this behavior are provided. The first one is due to the fact that the input oil concentration is very low in this layer (see Fig. 2(a)), as a result of the Eulerian–Lagrangian simulations reported in Starnoni and Manes (2022). In reality, it may be that some additional oil droplets reach the top layer, perhaps driven by a flow redistribution following the complete saturation of the lower sections of the filter. The second explanation is that, while the numerical saturation is averaged over the height of the respective layer, the experimental value is a punctual measure taken at its mid point, therefore the discrepancy is partly due to the small amount of oil which is driven downwards from the upper half of the upper layer and is not accounted for in the model. This small error can be easily smoothed out with increasing the discretization along the filter's height, however this would require a more complex parameterization of Eq. (16), which is beyond the scope of this work.

3.3.3. The network flow mechanism

So far, a number of clues have been collected that the oil transport processes inside the porous filter medium seemingly change after the second flow interruption, namely (i) the greater oil accumulation in the bottom section of the filter until the second flow interruption, (ii) the enhanced oil mobilization in the upper layers after the second flow interruption, and, as a consequence of (ii), (iii) a greater amount of oil retained inside the filter globally, respectively a slower film growth at the rear end of the bottom layer. It is the author's interpretation of the experimental evidence (and numerical results) that this change in oil dynamics is to be attributed to a major cause: the complete formation of the oil channels, in the Kampa-like sense, in the middle and upper sections of the filter.

To better illustrate these features, Figs. 7(a)–7(b) show the evolution of the oil mass inside the bottom and top sections of the filter, respectively. The internal oil mass of the jth layer, $M_{o,j}$, is calculated from the correspondent layer saturation $S_{o,j}$ as follows:

$$M_{o,j} = \rho_o(1-\alpha)S_{o,j}V_{F,j} = \rho_o(1-\alpha)S_{o,j}\pi D h_j L, \tag{26}$$

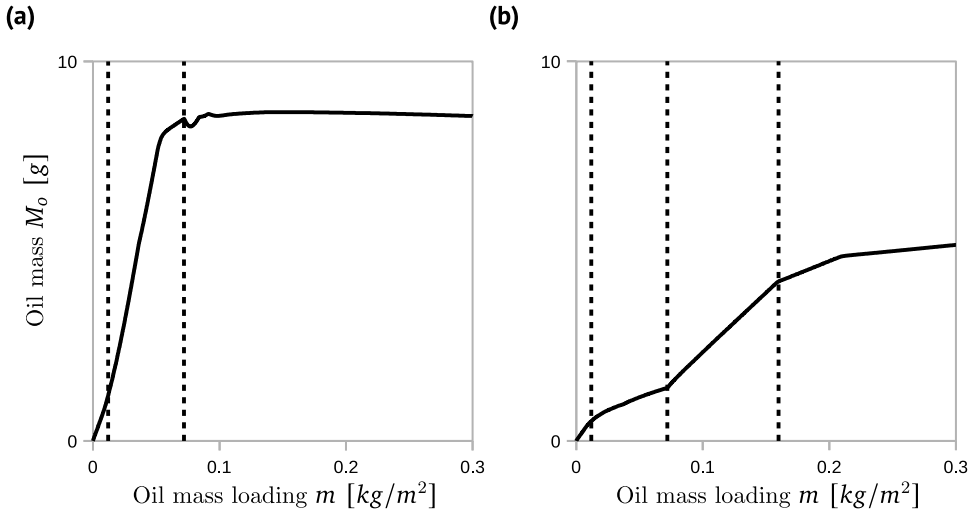

Fig. 7. Oil mass inside the bottom (a) and top (b) sections of the filter cartridge as a function of the oil mass loading. (a) Bottom section accounts for oil contained in layers 7, 8 and 9. (b) Top section accounts for oil contained in layers 1, 2, and 3. Oil mass within each layer is calculated using Eq. (26).

where $S_{o,j}$ is calculated using Eq. (25), $V_{F,j}$ is the volume of the jth layer, h_j and L are the height of the jth layer and filter's thickness, respectively, and D is the width of the filter in the direction perpendicular to the flow and to gravity, which is taken equal to the internal diameter (80 mm) of the filter cartridge of Liu et al. (2016). Note that the bottom oil mass in Fig. 7(a) is the sum of the oil contained in layers 7, 8 and 9, while the top oil mass in Fig. 7(b) comprises oil contained in layers 1, 2, and 3.

The most striking feature to note is that the oil content inside the bottom section is more than three times that of the top section until the second flow interruption (say, until $m = 0.072$ kg/m^2), as the oil progressively accumulates at the bottom of the filter due to gravity. Most interestingly, as Fig. 7(b) clearly shows, there are at least three changes in slope of the oil content curve within the top section. Now, it is known from the coalescence filtration literature that small kinks and changes in slope of a time evolution curve is a hint to a change in oil transport mechanism, e.g. from dust-like loading to channel flow, or from channel flow to film growth. Hence, the whole curve in Fig. 7(b) seemingly suggests the existence of an additional flow mechanism besides the conventional Kampa-like channel and film mechanisms. This additional mechanism is most likely characterized by movement of coalesced oil along multiple directions, say, both horizontally (driven by the pressure gradient) and vertically (driven by gravity), a scenario which is not contemplated in the original J&C model, where instead it is assumed that oil propagates as a vertical front in the direction of the air flow (Kampa et al., 2014).

The existence of this intermediate flow mechanism, which would not be properly understood within the framework of the original J&C model, is herein postulated, and the mechanism is termed 'network' indeed to put the emphasis on the multidimensional geometry of the oil patterns configuration. During this stage, a network of large filaments of coalesced oil is formed, which evolves, in a macroscopic sense, along the direction identified by S_M through the angle of coalescence θ defined in Eq. (15).

The existence of the intermediate 'network' stage might be the missing piece needed to address the three features identified at the start of this section and hence explain the saturation profiles detected in Liu et al. (2016). In particular, the network stage certainly initiates before the first flow interruption, as demonstrated by the oil accumulation in the bottom layers, and presumably lasts until some time between the second and the third flow interruption, culminating with the complete formation of the Kampa-like channels also in the top layers. Indeed, note in Fig. 6 that the curves corresponding to the first two flow interruptions are those featuring the more uneven saturation distributions, suggesting that channels are not yet established in the upper layers, with oil from those layers mainly migrating vertically towards the bottom section of the filter—feature (i).

At the end of the network stage, the complete formation of the channels produces an enhanced oil mobilization in the upper layers, resulting in detached coalesced oil to move horizontally within the same layer rather than draining downwards (due to gravity) towards the bottom section—feature (ii). Indeed, between the second and third flow interruption, the same top and middle layers all exhibit a distinct increase in slope of the saturation curve, as clearly illustrated in Fig. 6 and in aggregate form in Fig. 7(b). This in turn causes a greater rentention of oil inside the whole filter, thereby reducing the oil accumulation at the rear end of the bottom layer—feature (iii). This is also confirmed by the fact that, during the same time interval at which the saturation of the top layers increases, that of the bottom layers (say, P8 and P9) features a sudden drop in oil mass (caused by a drop in inflow oil mass from the upper layers), as clearly illustrated in Fig. 6. In the subsequent stages, the saturation remains steady in the bottom layer, where the equilibrium saturation is reached and pseudo-steady-state is locally established, while gradually increases from top to bottom. Global steady-state is reached after the fifth flow interruption (say, for $m > 0.2$ kg/m^2), as also illustrated in Fig. 5, although saturation keeps increasing steadily (but marginally in a global sense) in the top layer.

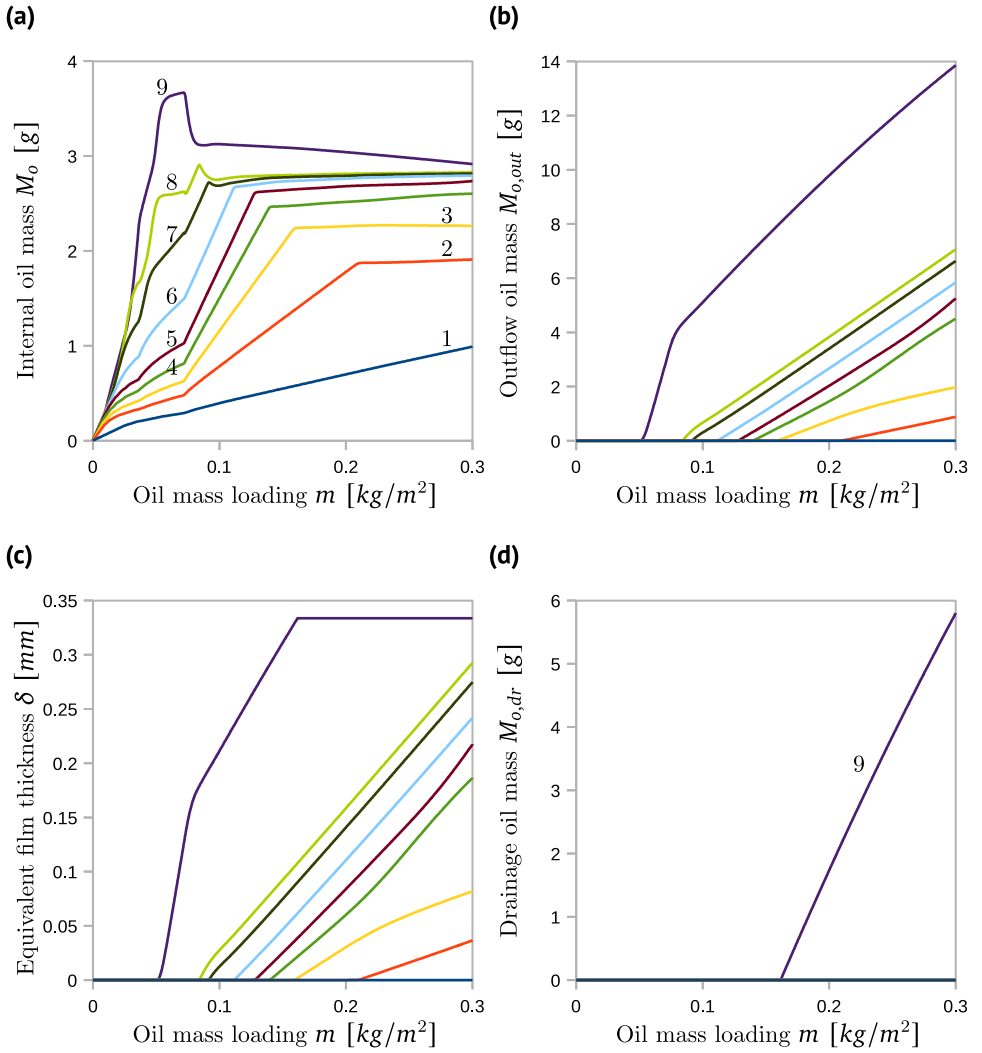

Fig. 8. Evolution of different oil content measures at different positions along the filter's height. (a) Internal oil mass M_o calculated using Eq. (26); (b) outflow oil mass $M_{o,out}$ calculated using Eq. (28); (c) equivalent film thickness δ calculated using Eq. (19); (d) drainage oil mass $M_{o,dr}$ calculated using Eq. (30).

3.4. Drainage volumes

Fig. 8 shows the evolution of different oil content measures during operation. Specifically, oil content is tracked in two forms throughout the calculations, namely internal oil, M_o, that is the amount of oil stored internally to the filter (in the form of saturation), and outflow oil, $M_{o,out}$, that is the amount of oil that has flown out from the filter. The latter is further split into two contributions, namely the oil film mass $M_{o,\delta}$, that is the amount of oil retained on the rear surface of the filter by capillary action, and the drainage mass $M_{o,dr}$, that is the amount of oil which has been effectively ejected out from the filter once that capillary forces have been locally overcome. The total oil mass $M_{o,\Sigma}$ is therefore given by

$$M_{o,\Sigma} = \sum_j \left(M_{o,j} + M_{o,out,j} \right) = \sum_j \left(M_{o,j} + M_{o,\delta,j} + M_{o,dr,j} \right), \tag{27}$$

where the sum is over the N_j layers. Fig. 8(a) shows the evolution of the internal oil mass $M_{o,j}$, which is calculated using Eq. (26), while Fig. 8(b) shows the outflow oil mass $M_{o,out,j}$, which for the jth layer is calculated as:

$$M_{o,out,j} = \rho_o V_{o,out,j}, \tag{28}$$

where $V_{o,out,j}$ is the correspondent outflow volume, calculated using Eq. (20). Recall $M_{o,out}$ is further split into two contributions, namely the oil film mass $M_{o,\delta}$ and the drainage mass $M_{o,dr}$. The former is calculated from the equivalent film thickness δ as

$$M_{o,\delta,j} = \rho_o \delta_j A_{F,j} = \rho_o \delta_j \pi D h_j \tag{29}$$

where δ_j is recorded throughout the computations using Eq. (19) and $A_{F,j} = \pi D h_j$ is the area of the jth rear surface. The drainage mass is given by continuity simply as

$$M_{o,dr,j} = M_{o,out,j} - M_{o,\delta,j}. \tag{30}$$

Figs. 8(c) and 8(d) report the evolution of δ_j and $M_{o,dr,j}$, respectively. The internal oil mass profiles reported in Fig. 8(a) are proportional to the saturations reported in Fig. 6(d), hence the same comments as detailed above apply. As far as outflow volumes are concerned, Fig. 8(b) shows that outflow through the rear surface of the filter initially occurs in the bottom layer only (some time between the first and second flow interruptions) and then gradually in the rest of the filter. Focusing on the bottom layer, Figs. 8(b)–8(d) clearly indicate the outflow pattern. Initially the oil film is formed, with the characteristics outlined in Section 3.2, specifically in Fig. 4(b). Then, when the oil accumulation is such that the exit capillary pressure is overcome, actual drainage occurs, whereby drainage is interpreted as breaking of the film (the equivalent thickness of which from then on is kept unchanged) and effective ejection of oil out from the filter. Indeed note the correspondence between non-zero drainage volumes and constant equivalent film thickness in Figs. 8(c)–8(d).

This analysis of drainage volumes is concluded with a qualitative comparison of the numerical results with the images of the outside surface of the filter cartridge as reported in Liu et al. (2016). For the top layer, there is no oil film (see Fig. 8(c)) as a result of the very low amount of oil mass which reaches this position. This is consistent with the visual observations of Liu et al. (2016), who report that little liquid is present on the outside surface of this position, and that the filter fabric could be clearly distinguished. The numerical oil film then generally increases from top to bottom. It is reported in Liu et al. (2016) that, at layer 5, most of the surface area is saturated by the liquid, while, at layer 9, the volume of the drained liquid increases more than that at the upper layers, and that the liquid film is thicker here. Layer 9 is indeed the layer where the drainage volumes are, by far, the highest over the entire filter (see Figs. 8(b)–8(d)). Most strikingly, Liu et al. (2016) report that bubbles simultaneously appear on the outside surface of layer 9, meaning that the gas flowed through the liquid film. This is indeed what Fig. 8(d) clearly indicates—that is, in layer 9, and there only, the exit capillary pressure is overcome and actual drainage through the oil film occurs. This demonstrates that the model represents the behavior of the porous filter medium quite well qualitatively, and is able to capture the important physical processes happening during operation.

3.5. Mass conservation and concluding remarks

As a final note, it is emphasized that mass conservation is ensured throughout the entire filtration process (both locally in the jth layer and globally), in the sense that the following mass balance is always satisfied:

$$M_{in} = M_{o,\Sigma}. \tag{31}$$

Here, $M_{o,\Sigma}$ is the total oil mass calculated using Eq. (27), while M_{in} is the total injected oil mass, which is computed as:

$$M_{in} = m A_F = m \pi D H, \tag{32}$$

where m is the mass loading per unit area and A_F is the total filter surface area. Fig. 9 reports this global mass balance. In particular, the total internal oil mass M_o coincides with the total injected mass M_{in} during the initial stage of wetting, then progressively deviates from linear once outflow begins to take place. Also note that the total outflow mass $M_{o,out}$ has eventually the same slope of M_{in} (say, M_o becomes constant), indicating that global steady-state has been reached—that is, oil drains out from the filter through its rear surface at the same rate at which it is loaded from its front surface.

In conclusion, the numerical results are consistent with the experimental observations of Liu et al. (2016) in that the lower section of the filter accumulates more oil mass and releases more oil outflow than the upper section during the filtration process. This is a result of the combined effects of non-uniform loading rates on the filter's front surface and internal oil redistribution within the filter driven by gravity, as discussed in Starnoni and Manes (2022) and properly modeled herein.

Furthermore, during the long exposition of this chapter, a number of clues has been collected that there likely is a change in oil transport processes after the second flow interruption, presumably determined by the complete formation of the Kampa-like channels in the upper section of the filter cartridge. This change in oil dynamics implies the existence of an additional intermediate stage which cannot be thoroughly understood within the framework of the original J&C model. This additional stage, which is characterized by movement of coalesced oil along multiple directions, say, both horizontally (driven by the pressure gradient) and vertically (driven by gravity), was termed 'network' indeed to put the emphasis on the multidimensional geometry of the oil patterns configuration. In the next section, a generalized Network, channel & film model is formulated, which extends the scope of application of the original J&C model by Kampa et al. (2014) to filters with coarser fibrous microstructure.

4. Formulation of the Network, Channel & Film model

4.1. The original J&C model

The original J&C model was firstly postulated in Kampa et al. (2014) and then formulated more extensively in Kampa et al. (2015). For an oleophilic material, it can be summarized in these terms: After the initial fiber loading, coalesced oil is transported through the filter by the air flow along multiple distinct parallel channels. When the coalesced oil reaches the rear surface of the

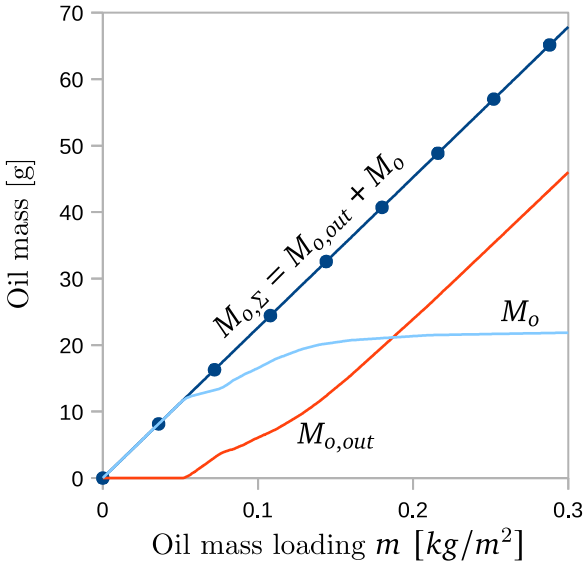

Fig. 9. Global mass balance during filtration – Eq. (31). M_o is the total oil mass inside the filter calculated as the sum of the jth Eqs. (26); $M_{o,out}$ is the total outflow mass calculated as the sum of the jth Eqs. (28); $M_{o,\Sigma}$ is the total oil mass calculated as the sum of M_o and $M_{o,out}$. Circles are the total injected mass calculated using Eq. (32).

filter, capillary forces retain the oil inside the medium and a thin liquid film is created, which produces a steep increase in pressure drop. When this jump pressure drop overcomes a critical threshold value, the oil breaks the thin film and exits from the filter, and pseudo steady-state is reached quasi instantaneously. For oleophobic media, the same two stages are observed, however in a reverse order—that is, with the jump preceding the channel stage.

Although the occurrence of these two distinct mechanisms is certainly not questioned here—it has been demonstrated by almost all experiments to date, the generality of the J&C model is still somewhat debated, as widely discussed in Starnoni and Manes (2022). This is because the filters studied in Kampa et al. (2014) (and following papers from the same research group) are limited to a certain type of filter media—that is, flat filters with a very dense fibrous microstructure (say, very low intrinsic permeability). For these type of filters, the porous fabric is such that the pressure gradient of the gas flow dominates over gravity and hence vertical flows are negligible. This is reflected by the fact that these authors report an almost homogeneous oil vertical distribution inside the filter. As a result, flow is essentially one-dimensional and coalesced oil is transported along multiple distinct parallel channels. The entire J&C model is indeed built on the assumption that liquid propagates as a vertical front in the direction of the air flow (Kampa et al., 2014).

On the contrary, the saturations detected for the vertical filter cartridge studied in Liu et al. (2016), which are replicated numerically herein, show an uneven vertical profile, with oil accumulating on the bottom section of the filter. As explained in Starnoni and Manes (2022), this is likely due to the combined effects of heterogeneous loading rates on the filter's front surface (caused by the heterogeneity of the complex flow fields developing in the interior of the filter cartridge) and internal gravity-induced flows. This clearly brings the filter cartridge studied by Liu et al. (2016) out of the scope of application of the original J&C model, and hence an extended formulation is sought.

4.2. The generalized Network, Channel and Film model

The generalized Network, Channel and Film model is illustrated in Fig. 10 and can be described as follows. Consider a sample of oleophilic fibrous material, initially at dry conditions (at time $t = t_0$), which is loaded at its front surface with a generated oil–mist. During the initial stage of loading, oil droplets deposit around the fibers as per effect of various capture mechanisms (impaction, interception, diffusion, etc.). This very initial stage is similar to dust filtration. When the amount of oil around the fibers is such that the fibers can no longer sustain its weight (say, at time $t = t_{detach}$), large droplets of coalesced oil start detaching from the fibers and moving inside the filter with their own motion. Following Darcy's law, the flow of this detached mass of coalesced oil is proportional to the pressure gradient of the mist and to gravity. Hence, a network of coalesced oil is formed which macroscopically evolves along the direction identified by the angle of coalescence θ as defined in Eq. (15). This means that, when $S_M \approx 1$, as for the filter cartridge studied by Liu et al. (2016), oil flow will occur along both directions, thereby leading to a greater oil accumulation on the bottom section of the filter. This mechanism is herein called "network" and occurs between t_{detach} and $t_{channel}$, where the latter is the time at which the Kampa-like channels are established through the entire filter's height—that is, from $t_{channel}$ onwards, oil propagates almost as a vertical front in the direction of the air flow. The network stage is identified in Fig. 11 with the first two changes in slope of the oil content curve within the top section of the filter.

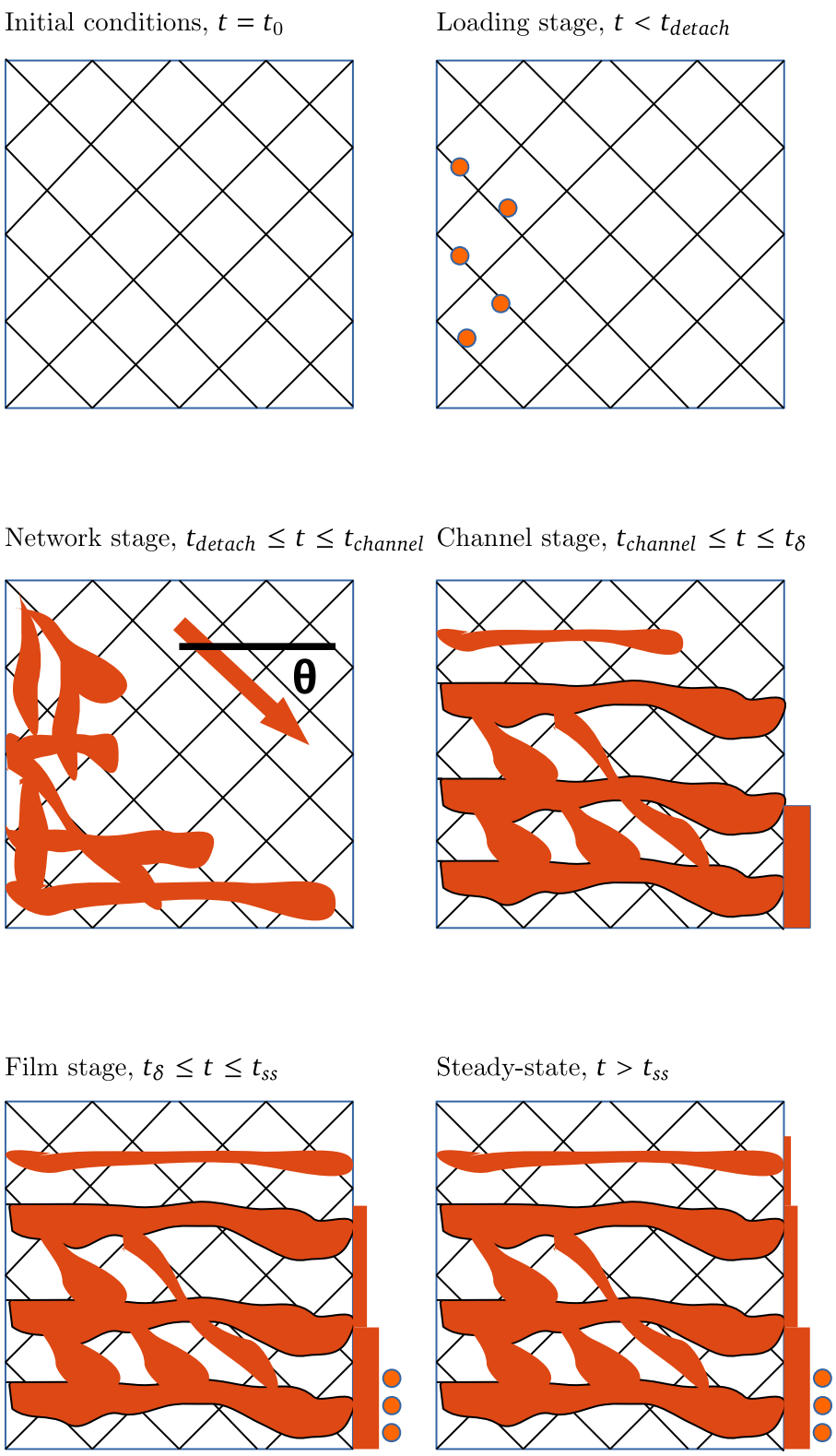

Fig. 10. Illustration of the generalized Network, Channel & Film model.

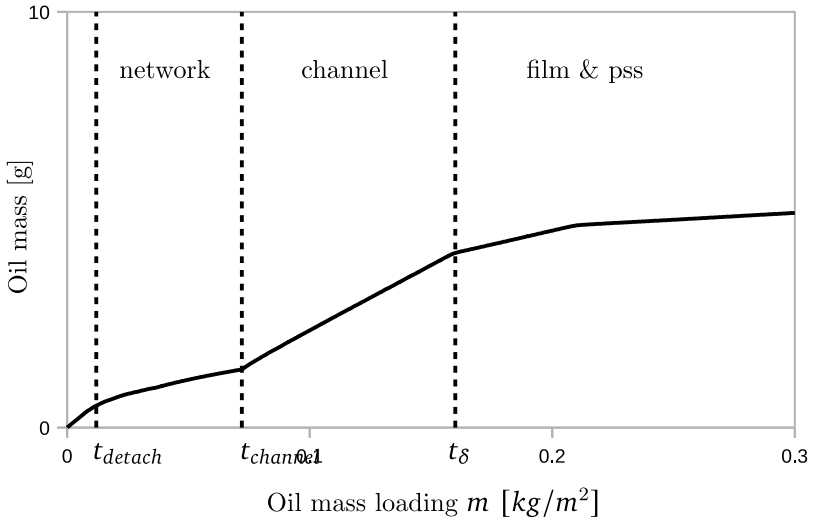

Fig. 11. Evolution of the oil mass inside the top section of a vertical filter cartridge – correspond to Fig. 7(b) – and schematization of the network, channel and film stages.

When, for $t > t_{channel}$, due to the increased oil saturation (and hence a reduction in the relative permeability of the gas phase), the pressure gradient becomes the dominant force, i.e. $S_M(t > t_{channel}) \gg 1$, the network naturally turns into a number of horizontal channels (as in the original J&C model), although some residual vertical flows are still present. Note that, when S_M is much greater than 1 already at dry conditions, as in the filters studied by Kampa et al. (2014), the network stage is not featured, and multiple parallel horizontal channels are established since the beginning of the coalescence flow, i.e. t_{detach} and $t_{channel}$ coincide in practice. For these type of filters, the network, channel and film model reduces to the original J&C model.

The remaining stages for $t > t_{channel}$ are the same as those featured in the original J&C model, with the important caveat that, while the "network" stage is considered at the global scale of the filter cartridge, the "film" stage is local to each position along the filter's height. In fact, when channel-like flow is initiated in the Kampa-like sense, each layer of the filter cartridge behaves almost as an independent 1D medium. Then, locally, the channel stage lasts until coalesced oil reaches the rear end of the filter and the oil film is created. This can occur at different times for each position along the filter's height. Indeed, as Figs. 7(a)–7(b) clearly show, the bottom section of the filter reaches pseudo-steady-state locally way earlier than the rest of the filter, specifically the bottom section reaches pseudo-steady-state about at the same time when oil channels begin to form in the upper section, that is in proximity of $t_{channel}$.

In this sense, at the global scale, the end of the channel stage is somewhat arbitrary and can be identified with the time at which the oil film is formed on almost the entire rear surface of the filter—in the present case, $t = t_\delta$ in Fig. 11 corresponds to the time at which the oil film begins to form at position 2 (see Fig. 8(c)). Eventually, when the oil film is formed everywhere along the filter's height, pseudo steady-state is globally established. However, as clearly illustrated in Fig. 9, global steady-state is in practice determined by the bottom layer only, which is where most of the oil accumulation occurs, and the only position where the local pressure drop overcomes the exit capillary pressure, effectively resulting in ejection of oil out from the filter cartridge (see also Fig. 8(d)).

5. Conclusions

A multidimensional model of oil–mist coalescence filtration through fibrous media has been presented, which extends the capabilities of previous models to the general case where 'channel-type' flow occurs in multiple directions, driven not only by the air flow but also from gravity. It was shown how the multidimensional model is able to replicate the results of an experimental setup available in the literature for which gravity-induced flow is a relevant mechanism, and for which the 1D approximation was shown to be insufficient to model the oil transport processes inside the porous medium.

An improved 'Network, Channel & Film' model was also formulated, which generalizes the original J&C model by Kampa et al. (2014) to filter with coarser fibrous microstructure such as those pertaining to industrially-relevant scenarios. In particular, the existence of an additional flow mechanism, called 'network', was postulated, which is characterized by a complex multidimensional oil patterns configuration spanning the entire filter's height and evolving, in a macroscopic sense, along the direction identified by the dimensionless number S_M. Evidence of how this generalized model explains the saturation patterns detected in Liu et al. (2016) was shown and discussed in thorough detail.

Notably, at the current state-of-the-art, the 'Network, Channel & Film' model can only be used to extrapolate a qualitative tendency of the flow regimes inside a filter cartridge. Although it was shown that it explains well the experimental setup of Liu et al. (2016), more experimental data are certainly needed in order to better quantify the transport phenomena within filter cartridges,

such as the relative importance of internal gravity-induced flows vs longitudinal drainage for intermediate values of S_M, the likely dependence of the duration of the network phase (until channel flow is established) on the oil loading rate, and the evolution of the spatial configuration of the oil channels. Nevertheless, the model seems to be useful, even though it is only formulated qualitatively for the moment, and more research is certainly needed to better characterize different types of filter media.

The limitations of the numerical model remain the same as those outlined in Starnoni and Manes (2021), specifically, it is imperative for future research to:

- Improve models for global equilibrium saturation S_e as a function of filter geometry and operational conditions, e.g. $S_e = S_e(\alpha, d_f, L, v_{in}, c_{in})$.
- Properly characterize the relevant material for better parametrization of the relative permeability functions, e.g. $\kappa_\alpha = \kappa_\alpha(s_\alpha)$.
- Carry out more research aiming at obtaining a relation linking the build-up of the pressure drop to the growing film thickness (and associated reduction in permeability), e.g. $K = K(\delta)$.
- Carry out more research into the dependence of the exit capillary pressure on the media structure, e.g. $\Delta p_{jump} = \Delta p_{jump}(\sigma, r_c, \text{contact angle})$.

To this end, a sensitivity analysis would be beneficial to explore deviations that may occur with different combinations of filter parameters, and might potentially be subject of a sequel paper.

A final remark concerns the integration of the generalized Darcy-scale model outlined in the present contribution and the turbulent Eulerian–Lagrangian simulations presented in Starnoni and Manes (2022) for the case of vertical filter cartridges with variable filter properties. Herein, constant-in-time oil loading rates on the filter's front surface were assumed. This is especially the case of relatively open-pore filter media like the one studied by Liu et al. (2016) and replicated herein. In this case, particle trajectories inside the filter cartridge are essentially unaltered during oil loading, since the capacity of the filter to accumulate oil is relatively scarce (saturation less than 1%), and therefore no significant changes in local filter's permeability are produced (the channel pressure drop is almost zero—see Fig. 4(b)). This effectively decouples external flow (i.e. turbulent flow in the interior of the cartridge) and flow inside the porous medium (i.e. darcian flow through the thickness of the filter medium). On the contrary, modeling vertical filter cartridges with very dense fibrous microstructure would be more difficult, since these filters have the capacity to accumulate great quantities of oil (saturations greater than 20%), hence significant changes of the filter's permeability would likely be produced, which in turn would induce changes in particle trajectories as the filter accumulates oil, these processes being strongly coupled. This integrated model poses severe challenges both computationally (multiscale simulation, unified software, etc.) and from a physical perspective (different flow regimes, timescales, etc.), and is currently under development.

Declaration of competing interest

The authors declare that they have no known competing financial interests or personal relationships that could have appeared to influence the work reported in this paper.

Data availability

Data will be made available on request.

Acknowledgments

I would like to thank Dr. Costantino Manes for his advice and valuable insight, as well as two anonymous reviewers for their useful comments.

References

Azarafza, A., King, A., Mead-Hunter, R., Schuler, J., Abishek, S., & Mullins, B. (2020). Prediction of residual saturation and pressure drop during coalescence filtration using dynamic pore network model. *Separation and Purification Technology*, *254*, Article 117588.

Baumann, A., Hoch, D., Behringer, J., & Niessner, J. (2020). Macro-scale modeling and simulation of two-phase flow in fibrous liquid aerosol filters. *Engineering Applications of Computational Fluid Mechanics*, *14*(1), 1325–1336.

Chang, C., Ji, Z., & Zeng, F. (2016). The effect of a drainage layer on filtration performance of coalescing filters. *Separation and Purification Technology*, *170*, 370–376.

Contal, P., Simao, J., Thomas, D., Frising, T., Callé, S., Appert-Collin, J., & Bémer, D. (2004). Clogging of fibre filters by submicron droplets. phenomena and influence of operating conditions. *Journal of Aerosol Science*, *35*(2), 263–278.

Kampa, D., Wurster, S., Buzengeiger, J., Meyer, J., & Kasper, G. (2014). Pressure drop and liquid transport through coalescence filter media used for oil mist filtration. *International Journal of Multiphase Flow*, *58*, 313–324.

Kampa, D., Wurster, S., Meyer, J., & Kasper, G. (2015). Validation of a new phenomenological jump-and-channel model for the wet pressure drop of oil mist filters. *Chemical Engineering Science*, *122*, 150–160.

Kolb, E., & Kasper, G. (2019). On the functioning of coalescence filters with a drainage layer–a comment on several papers by chang, others. *Separation and Purification Technology*, *225*, 54–59.

Kolb, H., Meyer, J., & Kasper, G. (2017). Flow velocity dependence of the pressure drop of oil mist filters. *Chemical Engineering Science*, *166*, 107–114.

Liu, Z., Ji, Z., Wu, X., Ma, H., Zhao, F., & Hao, Y. (2016). Experimental investigation on liquid distribution of filter cartridge during gas-liquid filtration. *Separation and Purification Technology*, *170*, 146–154.

Mead-Hunter, R., King, A. J., Kasper, G., & Mullins, B. J. (2013). Computational fluid dynamics (cfd) simulation of liquid aerosol coalescing filters. *Journal of Aerosol Science*, *61*, 36–49.

Mead-Hunter, R., King, A. J., & Mullins, B. J. (2014). Aerosol-mist coalescing filters–a review. *Separation and Purification Technology*, *133*, 484–506.

Raynor, P. C., & Leith, D. (2000). The influence of accumulated liquid on fibrous filter performance. *Journal of Aerosol Science*, *31*(1), 19–34.

Starnoni, M., Berre, I., Keilegavlen, E., & Nordbotten, J. M. (2019). Consistent mpfa discretization for flow in the presence of gravity. *Water Resources Research*, *55*(12), 10105–10118.

Starnoni, M., & Manes, C. (2021). A multiphase multicomponent flow and transport model for liquid aerosol filtration in coalescing fibrous filters. *Separation and Purification Technology*, *266*, Article 118574.

Starnoni, M., & Manes, C. (2022). On the interplay between pressure and gravitational forces in coalescing filters. *Journal of Aerosol Science*, Article 105953.